Optics & Laser Technology 199 (2026) 114941

Contents lists available at ScienceDirect

Optics and Laser Technology

journal homepage: www.elsevier.com/locate/optlastec

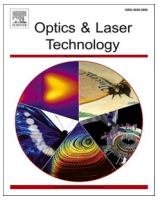

Full length article

Integration of PANI-SnO_2 heterojunctions with portable optical microfibre for advanced operando ammonia gas sensing

Hongtao Li [a,e,*], Wei Hu [a], Jiaoyan Dai [a], Shunshuo Cai [b,**], Lei Huang [a], Liang Lu [a], Jialiang Lv [a], Xue Liu [a,d], Feng Xu [a], Yujun Li [a,d], Benli Yu [a], Christophe Caucheteur [c]

[a] State Key Laboratory of Opto-Electronic Information Acquisition and Protection Technology, School of Optoelectronic Science and Engineering, Key Laboratory of Opto-Electronic Information Acquisition and Manipulation of Ministry of Education, Information Materials and Intelligent Sensing Laboratory of Anhui Province, Anhui University, Hefei 230601, China

[b] Microelectronics Instruments and Equipment R&D Center, Institute of Microelectronics, Chinese Academy of Sciences, Beijing 100029, China

[c] Electromagnetism and Telecommunications Department, University of Mons, Boulevard Dolez 31, 7000 Mons, Belgium

[d] Center of Free Electron Laser and High Magnetic Field, Anhui University, Hefei, Anhui 230601, China

[e] Institute of Environment, Hefei Comprehensive National Science Center, Hefei 230088, China

ARTICLE INFO

Keywords:
Optical microfibre
P-n heterojunctions
Gas sensing
NH_3 sensor
Rapid response
High sensitivity

ABSTRACT

In this work, we propose a synergistic framework between a p-n heterojunction and an optical microfibre for gas sensing, in which an n-type semiconductor, SnO_2, and a p-type semiconductor, polyaniline (PANI), form on surface of the optical microfibre at room temperature. Owing to the strong interaction between evanescent waves and carriers of semiconductors, the device could detect ammonia gas with a high sensitivity of 3.98 pm/ppm and an extremely low theoretical limit of detection (LOD) of 15.2 ppm. Importantly, its ultrafast response time is experimentally achieved at 11 s with a recovery time of 7 s, which is lower than those of most reported ammonia gas sensing technologies. Based on the proposed innovative integration of optical fibre with a p-n heterojunction sensing strategy, this work could provide a new way to promote more high-performance hybrid optical and semiconductor sensing platforms.

1. Introduction

Tracing analysis of ammonia gas molecules is important for preventing environmental and industrial pollution via the use of sensor-coated gas-sensitive materials [1–3]. In recent years, optical fibres coated with semiconductor materials have been proposed for the detection of gas molecules. Owing to their merits of microscale small size, low cost, flexible mechanical characteristics, and good portability, these optical sensors could be widely used in the detection of gas or liquid-related markers [4–16]. For example, tapered optical fibre ammonia gas sensors decorated with p-type or n-type semiconductor materials have attracted attention [17,18]. However, their detection sensitivities are not ideal. A long-period fibre grating (LPFG) device modified with delafossite $AgAlO_2$ was employed to detect ammonia gas with high sensitivity at room temperature, but the detection sensitivity was approximately 1 pm/ppm [19]. A tilted fibre Bragg grating sensor was used to evaluate the thickness and complex refractive index of the PANI nanofilm in ammonia gas environment, realizing a long response time of approximately 21 s [20]. A small-period LPFG sensor coated with poly(diallyldimethylammonium chloride)/poly(acrylic acid) for the detection of ammonia gas was realized, and the sensor realized a low ammonia gas sensing sensitivity of 2.74 pm/ppm and a high temperature sensing sensitivity of 8.7 pm/°C [21]. A LPFG sensor functionalized with a sol–gel silica film could detect ammonia with ultrahigh sensitivity, and its response and recovery times were as high as approximately 1 min and 10 min, respectively [22]. A high-cost single-mode fibre (SMF)-photonic crystal fibre (PCF)-SMF Mach-Zehnder interferometer coated with PANI-SnO_2 materials can achieve extremely narrow ammonia gas concentration detection ranging from 0 ppb to 8 ppb can be achieved [23]. With the development of high-performance low-

* Corresponding author at: State Key Laboratory of Opto-Electronic Information Acquisition and Protection Technology, School of Optoelectronic Science and Engineering, Key Laboratory of Opto-Electronic Information Acquisition and Manipulation of Ministry of Education, Information Materials and Intelligent Sensing Laboratory of Anhui Province, Anhui University, Hefei 230601, China.

** Corresponding author.

E-mail addresses: htli@ahu.edu.cn (H. Li), caishunshuo@ime.ac.cn (S. Cai).

https://doi.org/10.1016/j.optlastec.2026.114941
Received 23 December 2025; Received in revised form 2 February 2026; Accepted 9 February 2026
Available online 21 February 2026

dimensional materials, some two-dimensional (2D) material [24], MXene material [25], metal organic frameworks (MOF) material [26], nanofiber material [27] with remarkable merits of ultra-high specific surface area and tunable surface activity have been proposed for the application in various high-performance gas measurements. Take advantage of the above materials, optical fibres coated with 2D materials have been developed for the detection of ammonia gas in air in recent years. A SMF-hollow core fibre (HCF)-SMF-coreless fibre (NCF)-SMF sensor functionalized with graphene oxide was proposed for temperature compensation to sense ammonia gas with a sensitivity of 3.28 pm/ppm, a response time of 60 s and a recovery time of 30 s. On the basis of this design, the temperature crosstalk was effectively eliminated [28]. An optical microfibre coated with $Ti_3C_2T_x$ MXene-supported surface plasmon polaritons was employed to detect ammonia gas with a high LOD of 100 ppm [29]. A SMF-etched thin core fibre-SMF Mach-Zehnder interferometer with graphene/PANI was reported for detecting ammonia gas with a sensitivity value of 27.8 pm/ppm and a response time of 32 s[30]. Overall, although optical fibre sensors coated with p-type or n-type semiconductor materials can show good gas sensing performances, they also have drawbacks in some respects. For example, LPFG and TFBG devices have disadvantages of low sensing sensitivities, long response time, and high temperature sensitivity. Although PCF device can have high sensing sensitivity, their range of gas concentration detection was extremely narrow. Additionally, optical fiber sensors coated with single low-dimensional material can also have disadvantages of low detection sensitivities and long response times.

To address above issues, herein, we propose a new concept of joining p-n heterojunctions with low-cost and easily fabricated optical microfibre for application in gas-sensing areas at room temperature. Fig. 1(a) shows a schematic diagram of an optical microfibre integrated with a p-n heterojunction, which is composed of n-type SnO_2 and p-type PANI, for the detection of ammonia gas molecules. As shown in Fig. 1(a), if ammonia gas molecules are introduced into the system, the interfacial electrons on the surface of the nanocomposites can quickly move because their energy can overlap and interact with the large and strong evanescent field of our proposed optical microfibre. Fig. 1(b) illustrates the working mechanism of the dynamic reaction process of microscopic particles on the surface of the optical microfibre before and after the introduction of ammonia gas molecules into the proposed system. Owing to the combination of n-type SnO_2 with p-type PANI, a depletion layer with a certain value of electrical conductivity can be formed. Once ammonia gas molecules are introduced into the system, NH_3 molecules can undergo protonated polarization, resulting in the formation of NH_4^+. Moreover, the electrical conductivity of the p-n heterojunction and width of the depletion layer increase and decrease, respectively, in which the concentration of SnO_2 decreases because of the improved transformation of N^+ atoms from the PANI substrate centre to the depletion layer. Finally, the dielectric constant on the surface of the optical fibre changes. Owing to the dielectric constant modulation of the p-n heterojunction on the surface of the optical fibre within the evanescent field region, the monitored transmission spectrum can be redshifted with increasing concentration of ammonia gas molecules, as demonstrated in Fig. 1(c). This process can be described as follows:$PANI-NH^+ + NH_3(gas) \leftrightarrow PANI + NH_4^+$ [31]. Although other n-type materials (e.g. ZnO, TiO_2, In_2O_3, WO_3) can also be used, they have some disadvantages. Compared with ZnO, the SnO_2 can have better sensing stability in some moist environments. Compared with TiO_2, SnO_2 can have narrower bandgap and also work in room temperature. In_2O_3 material is high cost, and WO_3 can only work in high temperature environment. Thus, the SnO_2 is a best choice for using in this experiment..

A comparative analysis of existing fibre optic sensors based on p-n heterojunctions (e.g., the SMF-PCF-SMF interferometer in Ref. 27 and the graphene/polyphenyl modified SMF etched thin-core fibre in Ref. 30) have been proposed. However, they have drawbacks of narrow detection range of 0–8 ppb in Ref.27, slow response speed of 32 s in Ref. 30. The systematic analysis on the heterojunction-light field interaction have not been mentioned. In this work, the simultaneous optimization of sensitivity of 3.98 pm/ppm, response speed of 11 s/7 s for adsorption/desorption, and detection range of 0–500 ppm have been achieved on the basis of heterojunction-light field synergy mechanism. Comparing to other structural complicated optical fibres (e.g., PCF, etched thin-core fibre), our device can be possessed with low-cost and easy-to-fabricate configuration, which can enhance the practical application potential.

2. Results

2.1. Device fabrication and theory

The working principle of the fabricated optical microfibre is shown in Fig. 2 (a). The higher-order mode of HE_{12} and the fundamental mode of HE_{11} were separated and combined in the left and right transition regions, respectively. Thus, the Mach-Zehnder interferometric model

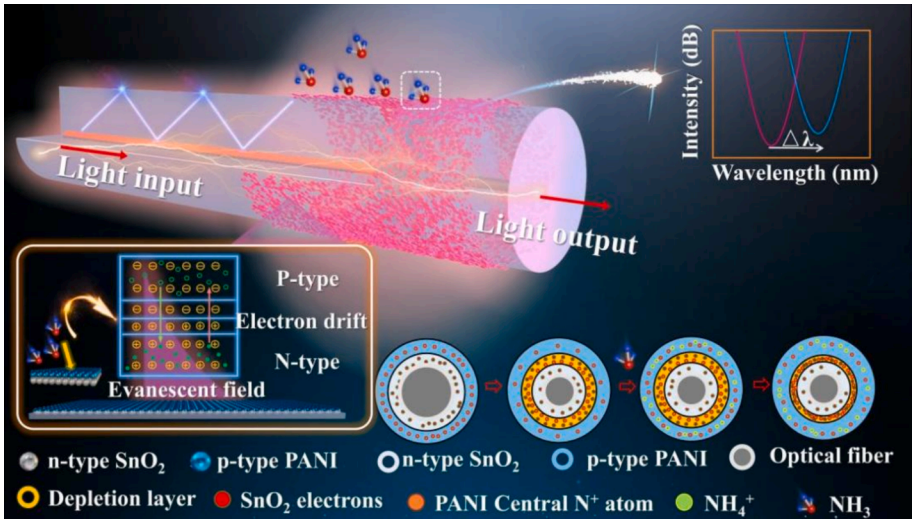

Fig. 1. (a) Schematic diagram of the optical microfibre platform coated with PANI-SnO_2 nanocomposites for the detection of ammonia gas molecules. (b) Working mechanism of the dynamic reaction process of microscopic particles on the surface of the optical microfibre. (c) Optical response of the optical fibre sensor to the target ammonia gas molecules.

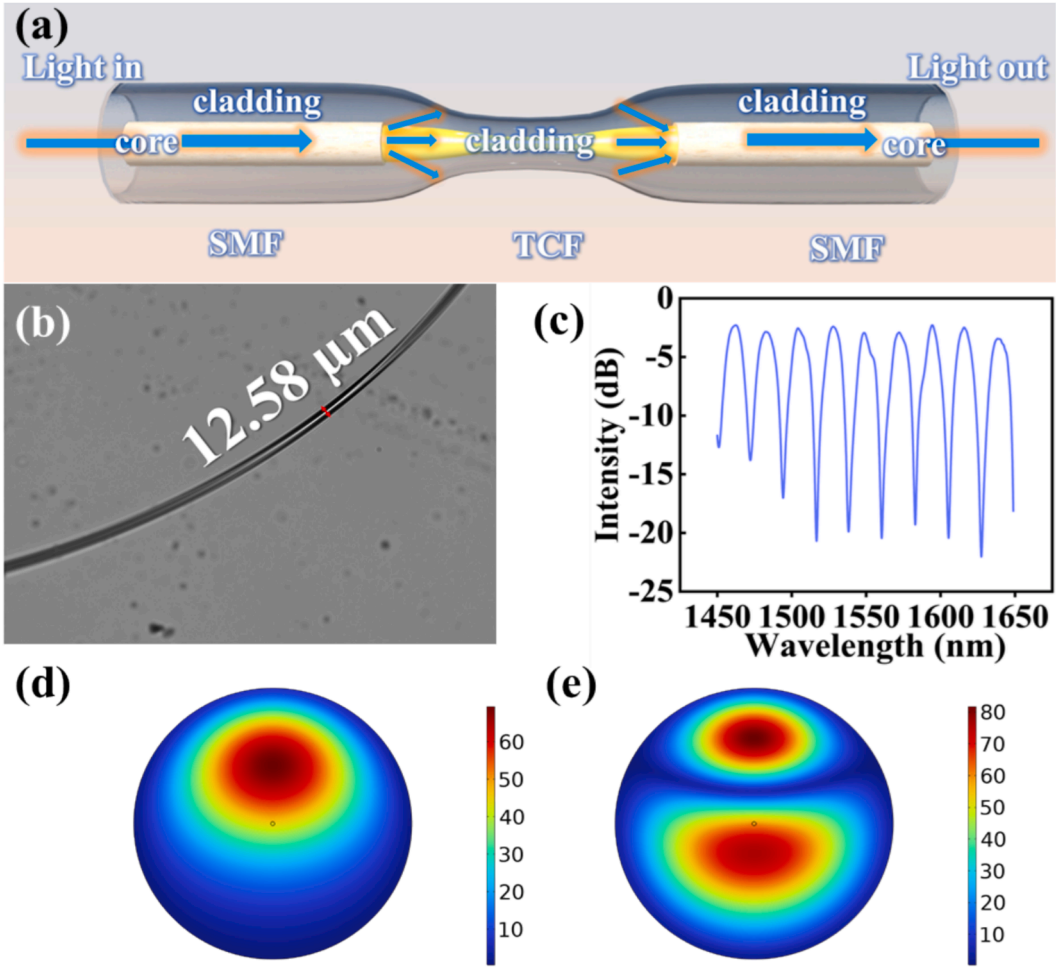

Fig. 2. (a) Schematic representation of the optical microfibre. (b) Optical image of the optical microfibre. (c) Measured optical transmission spectrum of the sensor device. Simulated (d) fundamental mode and (e) higher-order mode of the fabricated sensor device.

was created to generate the interference spectrum. The optical microfibre used in this experiment was fabricated via an automatic tapering system. A 1 cm-long thin-core fibre (TCF) was fusion-spliced to a SMF. Before tapering, the region of thin-core fibre was preheated for 1 min with a flame temperature of 2000 ℃.

After that, the diameter of optical fibre was gradually tapered by using hydrogen–oxygen flame fusion with a tapering speed of 3.5 mm/min, where the distance between optical fibre and flame gun was almost 8 mm. During this process, an optical spectrum analyzer (OSA) was used to monitor the transmission spectrum in real time. Finally, a microfibre with a diameter of 12.58 μm was fabricated. A real image of the fabricated optical microfibre can be shown in Fig. 2(b). The output transmission spectrum of the microfibre was recorded by using an OSA with a minimum resolution of 0.02 nm.The measured optical transmission spectrum of the sensor device is shown in Fig. 2(c). Because the high-order mode is highly sensitive to the refractive index of the optical microfibre surface, the interference spectrum exhibits a distinct wavelength shift with the variation of the surrounding refractive index at the uniform sensing region of the optical microfibre. The modal field distributions of the fundamental mode and the high-order mode were simulated and calculated via COMSOL Multiphysics, as shown in Fig. 2 (d) and (e), respectively. Specifically, a 2D axisymmetric model was established for the U-shaped optical microfibre with a core radius of 0.09 μm, a cladding diameter of 6.25 μm and a bending radius of 1 mm. The refractive indices of the core and cladding were set to be 1.4858 and 1.4444 at wavelength of 1550 nm respectively. Perfectly matched layers (PML) were applied at the edges of the simulation domain to eliminate light reflection interference, the wavelength of incident light was set to be 1550 nm.

2.2. *Construction of the p-n semiconductor sensing platform*

Owing to low cost and ammonia-specific characteristics, the PANI-SnO_2 nanocomposites can be considered as p-n heterojunction units in this fibre-optic sensing system. The procedure for modifying the PANI-SnO_2 nanocomposites p-n heterojunction units on the optical fibre is as follows: First, the prepared optical microfibre was cleaned with piranha solution, which contained 98% concentrated sulfuric acid solution and 30% hydrogen peroxide solution with a volume ratio of 7:3. At this time, the hydroxyl groups on the optical microfibre were exposed, and the scanning electron microscopy (SEM) image of smooth surface of the optical fibre is displayed in Fig. 3(a). Before the functionalization of the optical fibre, the immobilization conditions of PANI and SnO_2 solutions should be optimized. Gradient concentrations of 8%, 12%, and 15% were selected for the consideration of exploring the optimization condition of SnO_2 solution. Overly thick SnO_2 layer can be formed on the surface of fiber-optic with the optical fiber immersed in solution with concentration of 15%, which can significantly increase optical loss and disrupted the effective interaction between the evanescent field of the microfibre and the sensing layer. A continuous and dense coating on the fibre surface can not well formed with the optical fiber immersed in solution with concentration of 8%. Thus, the concentration of 12% can be considered as an optimal concentration for the SnO_2 solution. Next, PANI powder was dissolved in 1-methyl-2-pyrrolidinone (NMP) to

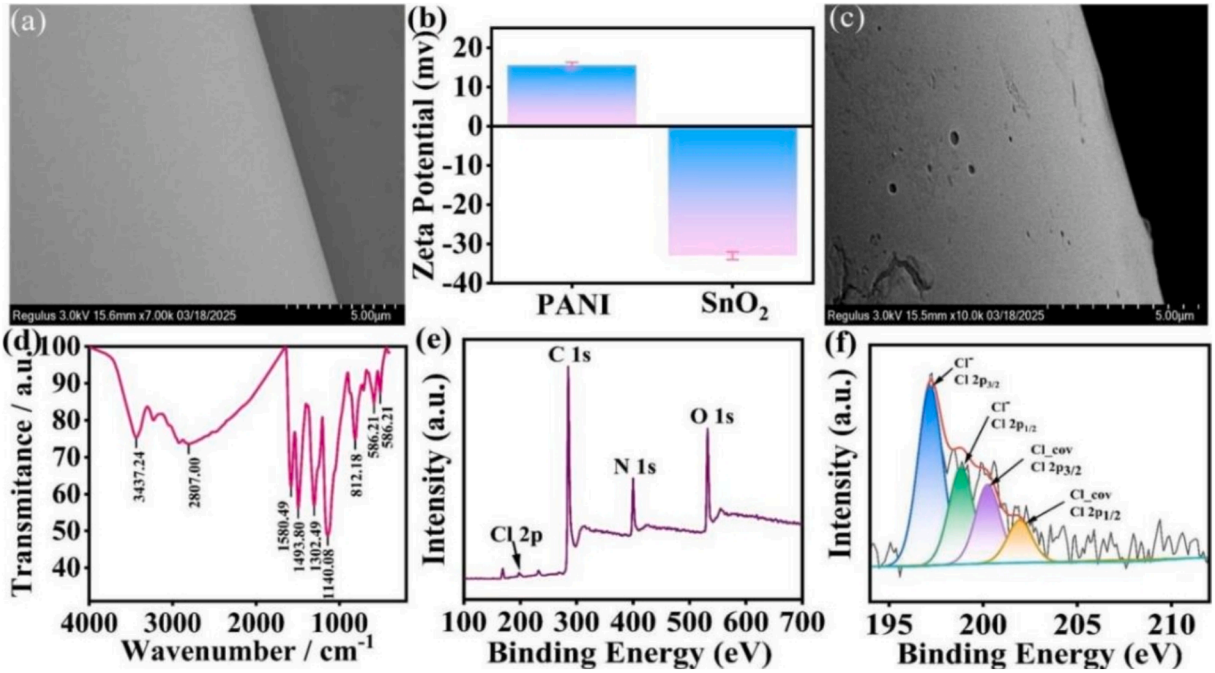

Fig. 3. (a) SEM image of the bare silica optical microfibre. (b) Zeta potential of the PANI and SnO_2. (c) SEM image of the optical microfibre coated with SnO_2. (d) Fourier transform infrared spectroscopy of the PANI layer. (e) and (f) X-ray photoelectron spectroscopy analysis of the PANI material.

prepare solutions with gradient concentrations of 1 mg/mL, 3 mg/mL, and 5 mg/mL. The solution of 5 mg/mL concentration can induce severe agglomeration of PANI molecules, leading to an uneven coating structure. This can not only lead to additional optical scattering loss but also cause blurred spectral dips, making it impossible to accurately track wavelength shifts during gas sensing. When the optical fibre sensor was immersed into solution with concentration of 1 mg/mL, its surface could not form a complete sensing layer, resulting in weak interaction of the sensor with ammonia gas molecules. Therefore, 3 mg/mL can be considered as an optimized concentration for the PANI solution. In addition to concentration optimization, the zeta potentials, pH values, and ionic strengths of the optimized PANI and SnO_2 solutions were characterized to verify the feasibility of electrostatic adsorption between the two materials. As shown in Fig. 3(b), the zeta potentials of PANI and SnO_2 were measured at −34.1 mV and 16.2 mV, respectively, indicating electrostatic attraction between the negatively charged PANI and positively charged SnO_2, which facilitates the formation of a stable heterojunction. The pH values of the PANI and SnO_2 solutions were 10.0 and 3.7, respectively, and the ionic strengths were consistent with the optimized concentrations (12% for SnO_2 and 3 mg/mL for PANI). Afterwards, the SnO_2 nanomaterial can be successfully immobilized onto the surface of optical fibre, which can be verified by the morphological presentation of the SEM result (Fig. 3(c)). Actually, the provided Fourier transform infrared (FTIR) spectroscopy and X-ray photoelectron spectroscopy (XPS) data were specifically intended to characterize PANI oxidation state, doping method, or molecular structure. The oxidation state of the sample was clearly confirmed by the FTIR spectrum (Fig. 3 (d)). The intermediate oxidation state of PANI for the emeraldine salt form exhibited following typical infrared characteristic peaks: the absorption peak at 1493 cm^{-1} was assigned to the C=C stretching vibration of the benzoid structure (B, representing the reduced unit), and the peak at 1580 cm^{-1} corresponded to the C=C stretching vibration of the quinoid structure (Q, representing the oxidized unit). As clearly shown in the figure, the intensities of two peaks were comparable, and the B/Q peak intensity ratio was a key indicator for determining the oxidation state of PANI. The simultaneous presented two peaks with similar intensities could directly prove that the sample was in the intermediate oxidation state, which was highly consistent with the standard FTIR spectrum of emeraldine salt.

The XPS data (Fig. 3(e) and 3(f)) provided conclusive evidence for the doping method and molecular structure. The XPS survey spectrum (Fig. 3(e)) clearly showed the characteristic photoelectron peaks of C 1s, N 1s, O 1s, and Cl 2p. The presence of the Cl 2p peak directly confirms that chlorine (Cl) has been successfully introduced into the PANI molecular chain, verifying that the dopant was hydrochloric acid (HCl). The high-resolution Cl 2p XPS spectrum further revealed the chemical state of Cl (Fig. 3(f)). Typically, the Cl 2p spectrum could be deconvoluted into two pairs of spin–orbit doublets (Cl $2p_{3/2}$ and Cl $2p_{1/2}$), and their peak separation could be fixed at 1.6 eV. The doublet corresponding to characteristic of ionic Cl^- was attributed to the Cl^- counterions bonded to the imine nitrogen atoms on the PANI chain. H^+ provided by the protonic acid protonates the imine nitrogen atoms, while Cl^- embedded between the chains as counterions to maintain electrical neutrality, ultimately forming a conductive emeraldine salt structure. The other pair of doublets with lower binding energy may originated from a small amount of covalently bonded chlorine or adsorbed chlorine species. In summary, the comprehensive analysis of the FTIR and XPS spectra demonstrated that the prepared sensing material was HCl-doped PANI in the intermediate oxidation state, it had a typical emeraldine salt-type molecular structure.

In the next step, the SnO_2 nanosheets and PANI nanosheets were sequentially immobilized onto the fibre-optic surface via electrostatic force by optimizing the decoration time and concentration of the two solutions. In order to investigate the deposition kinetics of two materials on the surface of optical fibre, their SEM images and optical-response procedures should be considered. Fig. 4(a)-4(g) depict the morphological and optical signal envelopment of the PANI coated on the surface of optical fibre. From twenty minutes to sixty minutes, the degree of roughness of optical fibre surface in three SEM images can be increased (Fig. 4(a), Fig. 4(c), Fig. 4(e)).

At the same time, the transmission spectrum can be gradually red shifted in Fig. 4(b), Fig. 4(d), Fig. 4(g). Therefore, the PANI-SnO_2 thin film was successfully formed on the optical fibre. To provide macroscopic evidence for the formation of a p-n heterojunction, we conducted cross-sectional SEM analysis. As shown in Fig. 4(f), the thicknesses of the SnO_2 and PANI film layers were measured at 260 nm and 130 nm,

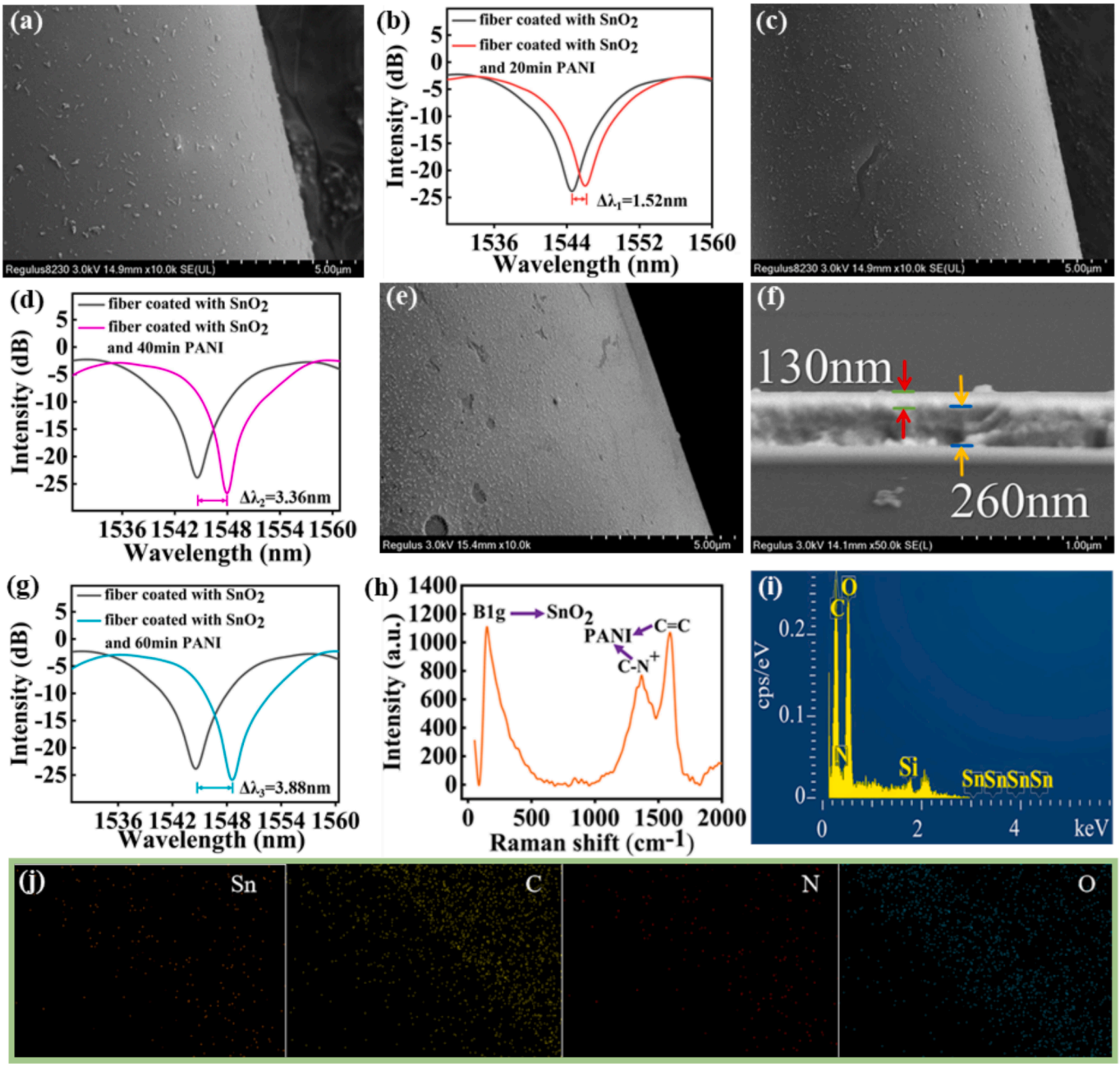

Fig. 4. SEM images of degree of roughness of optical fibre surface in PANI solution for (a) twenty minutes, (c) forty minutes, (e) (f) sixty minutes. The variations of transmission spectrum of the optical fibre sensor in PANI solution for (b) twenty minutes, (d) forty minutes, (g) sixty minutes. (h) Raman spectrum of the nanocomposites. (i) EDS spectrum of the nanocomposites on the optical microfiber. (j) EDS elemental mapping of Sn, C, N and O for the optical microfiber with uniformly dispersed nanocomposite particles.

respectively. Raman spectroscopy (Fig. 4(h)) also displays the characteristic peaks of PANI and SnO_2, which indicate the coexistence and interaction of both materials at the interface of optical fiber. Fig. 4(i) and 4(j) present the energy dispersive X-ray spectroscopy (EDS) spectrum of heterojunction and their corresponding elemental mapping. In Fig. 4(j), Sn element in SnO_2 is uniformly dispersed on the optical microfiber surface. The distribution area of Sn highly overlaps with those of C and N elements in PANI, and O element in SnO_2 and PANI, directly verifying the successful loading of Sn element in SnO_2 in the composite coating. The characterization results confirm that SnO_2 and PANI have been successfully combined on the surface of the optical microfibre, and a p-n semiconductor film has been successfully constructed, which is applicable for ammonia gas molecule detection.

2.3. Gas sensing behaviour and temperature properties of the device

Fig. 5(a) shows the experimental setup for ammonia gas sensing. As shown in the figure, the as-prepared optical microfibre probe was sealed in a gas chamber. The incident light was launched from a broadband source (BBS) with a spectral range from 1250 nm to 1650 nm. At the same time, an OSA was employed to monitor the spectrum evolution of the device in real time. To systematically evaluate the sensing sensitivity, ammonia gas with concentrations ranging from 0 ppm to 500 ppm was sequentially injected into the chamber, and the transmission spectrum was recorded in real time. Specifically, the response value ($\Delta\lambda$) of the sensor is defined as the difference between dip wavelength of λ_1 and dip wavelength of λ_2. λ_1 represents the dip wavelength of the sensor after

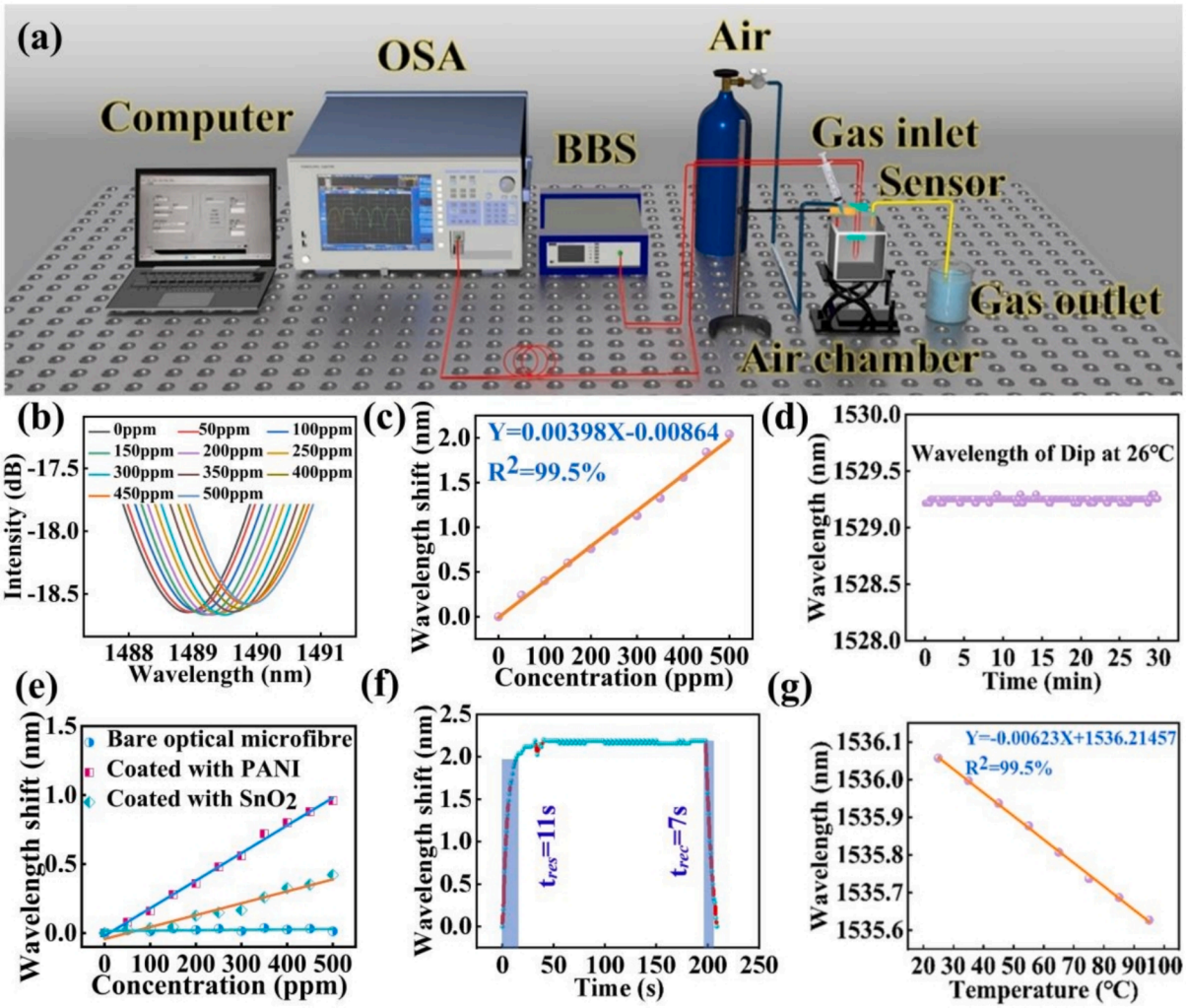

Fig. 5. (a) experimental setup of the ammonia gas sensing system, (b), (c) optical response of the sensor to ammonia gas at different concentrations, (d) spectral stabilization of the sensor in ammonia gas at a concentration of 250 ppm, (e) optical responses of bare optical fibre, fibre coated with only PANI, fibre coated with SnO_2 to ammonia gas with different concentrations, (f) response and recovery times of the device, (g) optical response of device to temperature.

exposure to a specific concentration of ammonia gas, and λ_0 denotes the initial dip wavelength measured in dry air. By linear fitting of the dip wavelengths of the device, we obtained a high linear fitting value of 99.5% and a detection sensitivity of 3.98 pm/ppm (Fig. 5(c)). According to numerical calculations, the standard deviation of s_1 was derived at 0.0172853 nm (Fig. 5(d)). By inscribing the above numerical results of sensitivity and x_1 into the equation: $x_{LOD} = f^{-1}(3\sigma_1)$ [32,33], Combining the yellow line from Fig. 5(c),$f(x) = 0.00398x - 0.00864$, thus, the theoretical limit of detection (x_{LOD}) was calculated to be 15.2 ppm. To evaluate the role of the p-n heterojunction in enhancing sensing performance, bare optical fibre, fibre only coated with PANI, fibre only coated with SnO_2, and the fiber coated with PANI-SnO_2 heterojunction were applied to ammonia gas with different concentrations in Fig. 5(e). As shown in Fig. 5(e), the bare microfiber exhibits an extremely low sensitivity of 0.027 pm/ppm, confirming its negligible intrinsic response to ammonia gas. When the optical microfibre only modified with SnO_2, the sensing sensitivity can increase to be 0.863 pm/ppm. When the optical microfibre only coated with while the PANI, the sensor can also show a low sensing sensitivity of 2.0 pm/ppm. Hence, the sensor coated with only one material can show the limited sensing capability, which are attributed by their restricted carrier modulation and inefficient interaction with ammonia molecules. In contrast, the optical microfibre coated with PANI-SnO_2 heterojunction can achieve a significant sensitivity of 3.98 pm/ppm, which is approximate 4.6 times higher than that of SnO_2 and 2.0 times higher than that of PANI. Therefore, above experimental results can fully demonstrate the existence of PANI-SnO_2 heterojunctions in our sensing system. Ammonia gas with a concentration of 500 ppm was injected into the chamber, and the device could absorb ammonia gas molecules with a fast response time of 11 s. Herein, the response time can be defined that dip wavelength of the sensor's transmission spectrum reached to 90% of the total redshift after the injection of ammonia gas into the test chamber (Fig. 5(f)). After the reaction, dry air quickly flowed into the chamber, by recording this recovery process, we obtained a recovery time of 7 s. Herein, the recovery time can be defined that the dip wavelength returned to 10% above the initial baseline after flushing dry air into the chamber to remove ammonia (Fig. 5(f)). In some real measurement scenes, temperature variations usually occur, which could easily reduce the measurement accuracy of the device. Therefore, it is necessary to consider the temperature sensitivity characteristics of the optical microfibre. When the temperature was changed from 20 °C to 100 °C, the temperature sensitivity of the device was calculated to be as low as −6.23 pm/°C (Fig. 5(g)). This negligible temperature-induced spectral shift demonstrates the sensor's excellent overall performance. Its outstanding temperature stability allows it to consistently maintain high measurement accuracy even in environments with fluctuating temperatures.

2.4. Specificity, repeatability, and shelf-life of the device

Fig. 6(a) shows the optical response of the as-prepared optical microfibre to ammonia gas and other types of gas molecules. Owing to the high specificity of the sensor device, ammonia gas at a concentration of 500 ppm can induce a large wavelength shift of 2.08 nm. In contrast, very low values of the wavelength shift of the optical fibre are induced by control gas molecules. For the mixed gas sensing test, the mixed gas was formulated with all the specific target gases involved in the single gas sensing test, and the concentration of each gas in the mixed system was uniformly set to be 500 ppm. The ammonia gas molecules in the mixture of gas molecules can also be effectively found by using our fabricated optical microfibre device (Fig. 6(a)) p-n semiconductor materials could distinguish target gas molecules well from other control types of gas molecules. Fig. 6(b) shows the optical response of the device to mixed gases during the entire response and recovery process. As shown in the figure, the response and recovery times of the sensor in mixture gas were measured at 14 s and 8 s, respectively. Fig. 6(c) shows the optical response of the sensor to pure ammonia gas at concentrations ranging from 50 ppm to 500 ppm on the basis of ten-times different measurement cycles. In Fig. 6(c),we have counted out response times of 17 s, 15 s, 12 s, 11 s, which are corresponding to the ammonia gas concentration of 50–100 ppm, 150–200 ppm, 250–400 ppm, 450–500 ppm, respectively. Thus, the concentration of ammonia gas can affect the response time, and the sensor also shows good performance after ten-times cycles. The sensor in different relative humidity (RH) environments have been investigated in Fig. 6(d). For controlling humidity during this gas sensing experiment, the conventional saturated salt solution humidity control method was strictly adopted [34]. Different saturated salt solutions were placed in the sealed test chamber to achieve accurate and stable regulation of the environmental relative humidity inside the chamber. The test environments with different humidity levels were constructed as follows: 0% RH was achieved by purging the test chamber with dry air, while 50% RH and 95% RH were established by placing saturated aqueous solutions of $Mg(NO_3)_2$ and KNO_3 inside the chamber, respectively. In NH_3 with concentration of 250 ppm, the optical response ability and recovery performance can be gradually reduced with the increased RH values, that demonstrating the reaction suppression of materials by water molecules.

Fig. 6(e) shows the optical response of the sensor to ammonia gas at different concentrations on the basis of three independent experiments. The above results further prove that the sensor can have excellent repeatability in ammonia gas sensing measurements. Three additional concentrations (700 ppm, 900 ppm, and 1000 ppm) were tested beyond 500 ppm, revealing that the sensing performance tends to saturate. Within the ammonia gas concentrations ranging from 0 ppm to 500 ppm, the sensor could also maintain a high sensitivity of 3.98 pm/ppm and a linear correlation coefficient of 99.5%. This range is significantly wider than that of most reported high-sensitivity fibre-optic ammonia gas sensors in recent years. For example, the graphene/PANI-modified SMF-TCF-SMF interferometer had a detection range lower than 100 ppm. the $AgAlO_2$-modified LPFG sensor had a detection range lower than 200 ppm, and most of these sensors suffer from limitations of slow response speeds, and their applicability were only used in ultratrace scenarios.

Meanwhile, the upper limit of 500 ppm fully covered the concentration requirements of mainstream real-world application scenarios. For instance, the occupational safety thresholds for ammonia gas specified by Occupational Safety and Health Administration (OSHA) are Permissible Exposure Limit (PEL) for 50 ppm and Immediately Dangerous to Life or Health (IDLH) for 300 ppm. The ambient air quality guideline is recommended by World Health Organization (WHO) is 100 ppm. The typical concentration ranges in scenarios such as agricultural and livestock farming are 50–400 ppm generated by manure decomposition. Early leakage of ammonia gas refrigerants are 100–500 ppm induced by food/pharmaceutical cold chain storage. The system enables

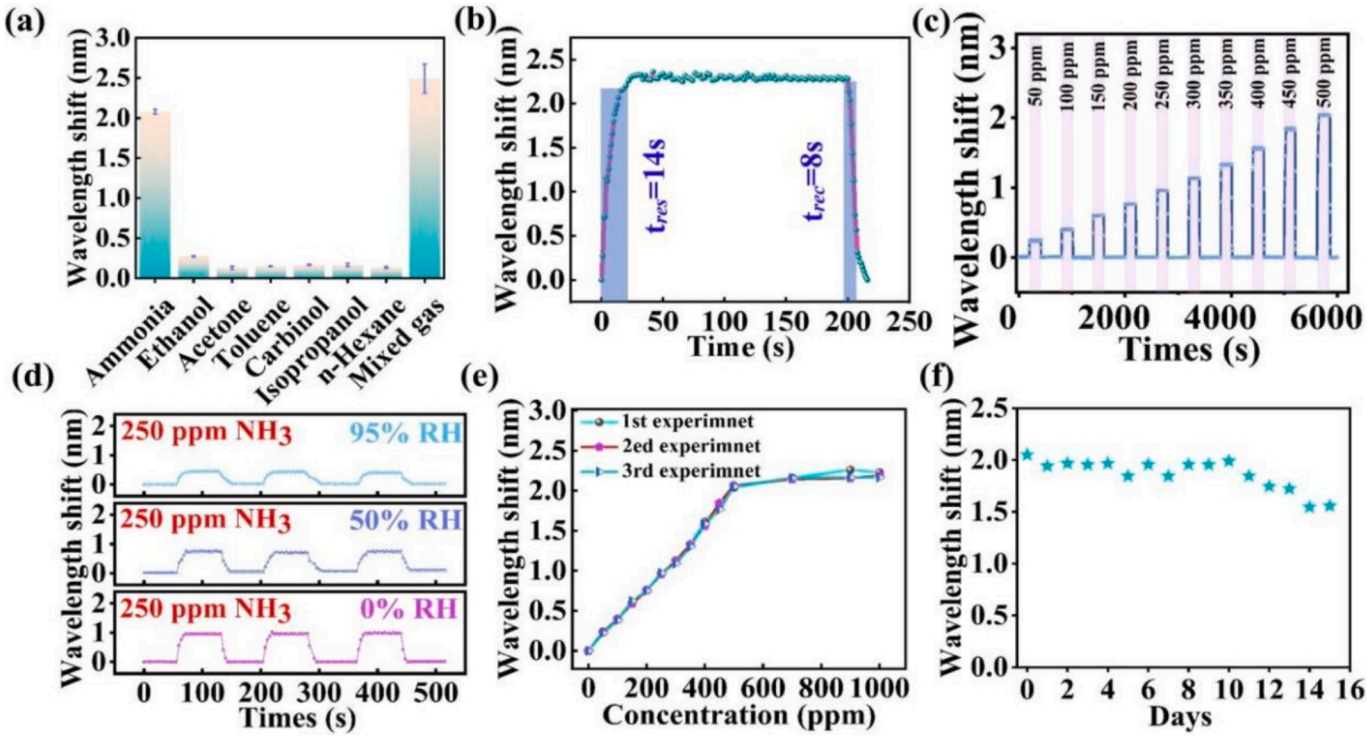

Fig. 6. (a) Specificity of the sensor. (b) response and recovery characteristics of the device in mixture gas. (c) optical response of the sensor to pure ammonia gas at concentrations ranging from 50 ppm to 500 ppm on the basis of ten independent measurement cycles. (d) optical response of the sensor to ammonia gas in different RH environments. (e) optical response of the sensor to ammonia gas with different concentrations on the basis of three independent experiments. (f) shelf life of the optical microfibre with nanocomposites.

safety early warning and real-time monitoring, which can meet the needs of the vast majority of practical applications.

Fig. 6(f) shows the shelf-life of the optical microfibre coated with the SnO_2 and PANI nanocomposites. Within thirteen days, the as-prepared sensor can detect ammonia gas without considerable optical loss. However, after thirteen days, the SnO_2 and PANI nanocomposites on the sensor gradually attenuated, resulting in relatively large optical losses in the integrated device. In order to improve shelf life of the device in out-of-lab scenarios, there are two methods as following: 1. The introduction of specific functional groups on the main chain of PANI may enhance its chemical stability. 2. Fabrication of three-dimensional porous SnO_2 or doping noble metal nanoparticles into SnO_2 may enhance physical and chemical stability.

3. Discussion

Although the aforementioned evanescent wave-based optical sensing experiments convincingly demonstrate the superior gas-sensing performance of the SnO_2-PANI nanocomposite, the underlying improvement mechanism requires clarification. To elucidate the charge carrier dynamics at the p-n heterojunction interface on the optical fiber device, we developed a model system consisting of an optical microfiber coated with sequentially deposited SnO_2 and PANI films. Two microelectrodes were fabricated on this coated fiber to enable direct electrical probing.

The operating principle of this p-n heterojunction-integrated optical fiber, before and after ammonia exposure, is illustrated in Fig. 7(a) and 7 (b), respectively. Initially, contact between n-type SnO_2 and p-type PANI creates a p-n junction with a built-in electric field and a charge depletion region at their interface, as shown in Fig. 7(a). Upon exposure to ammonia, the reducing gas molecules donate electrons to p-type PANI, decreasing its hole concentration. This causes the Fermi level (EF) of PANI to shift downward, increasing the work function difference (ψ_{bi}) and the junction barrier height. Consequently, the depletion region, particularly on the PANI side (W_p), widens substantially, driving the composite into a high-resistance state at room temperature. This change in resistance directly corresponds to a decrease in the effective electrical conductivity (x) of the nanocomposite coating. The interfacial refractive index (n_{sur}) of the microfiber, which governs evanescent field interaction, is influenced by the complex dielectric properties of the coating. For the PANI-SnO_2 composite, the real part of the dielectric constant (ε) is related to x. As x decreases upon gas exposure (due to increased resistance), ε and consequently n_{sur} are modulated. This mechanism allows our optical microfiber-integrated p-n junction to efficiently translate ammonia concentration into measurable optical signal variations (e.g., intensity or wavelength shift), enabling ultrasensitive and rapid detection.

The band gaps of the materials were determined using Tauc plot analysis of optical absorption data. The direct band gap (E_g) was obtained from the equation [35–37]:

$$(\alpha h\upsilon)^2 = A(h\upsilon - E_g) \quad (1)$$

where α is the absorption coefficient, $h\upsilon$ is the photon energy, and A is a constant. To experimentally validate the electrical behavior of the semiconductor heterojunction on the microfiber, we monitored real-time current changes. Fig. 7(c) shows the probe station setup. When incident light (1250–1650 nm) was introduced, the electrical current remained stable, indicating a steady-state depletion region under illumination (Fig. 7(d)). Upon introducing 500 ppm ammonia, the current decreased significantly (Fig. 7(e)), corresponding to an increase in system impedance due to the widening of the depletion layer. This confirms that our electro-optical composite waveguide can effectively monitor minute electrical perturbations on the fiber surface, translating them into a robust sensing signal.

A performance comparison between reported works and our work is presented in Fig. 8(a) and 8(b). As shown in Fig. 8(a), our proposed optical microfibre coated with PANI-SnO_2 has ultrafast response and recovery times compared to optical fibres decorated with p-type or n-type semiconductor materials. Although researchers have realized much faster response or recovery times in Ref.23, its detection range and sensing sensitivity, as shown in Fig. 8(b), need to be improved. As shown in Fig. 8(b), although the SMF-TCF-SMF structure in Ref. 26 could achieve ultrahigh detection sensitivity, its detection range was narrowed to within 100 ppm. Our proposed method not only has high sensing sensitivity but also possesses a remarkably wide detection range.

It should be noted that the PANI/SnO_2 p-n heterojunction structure validated in this work also lays a foundation for potential performance enhancement via photoelectric synergy. As documented in the literature, under light illumination, such a heterojunction interface can effectively promote the separation of photogenerated electron-hole pairs [38]. The injection of these photogenerated carriers can further modulate the surface energy states and the concentration of active sites [39], thereby potentially significantly enhancing the adsorption and reaction kinetics towards target gases. This has been confirmed as an effective

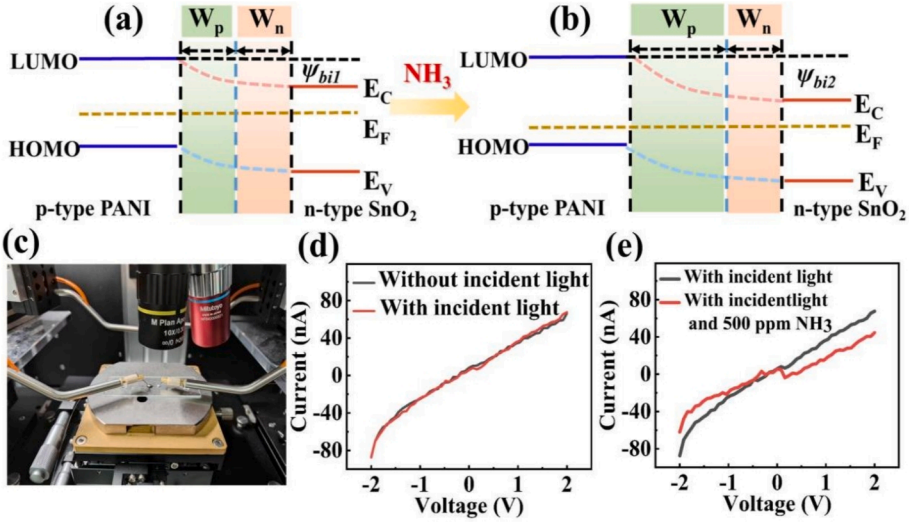

Fig. 7. (a) Before and (b) after introducing ammonia gas molecules into the system. (c) Physical illustration of the constructed fibre–optic semiconductor measurement system; different electrical signals of the p-n semiconductor on the surface of the optical microfibre are measured before and after introducing.(d) incident light and (e) ammonia gas at a concentration of 500 ppm.

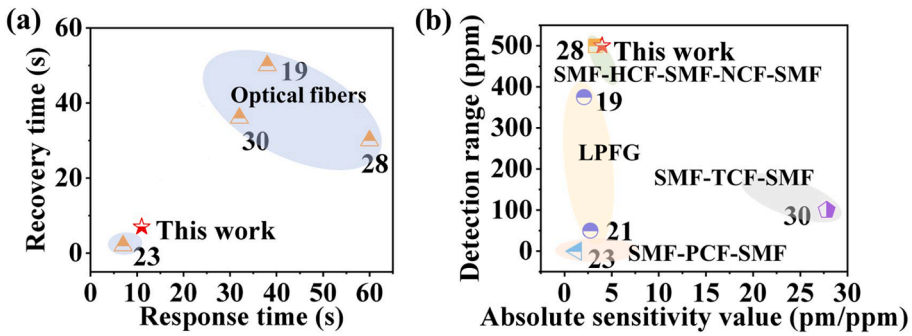

Fig. 8. Comparison of (a) response/recovery times (b) absolute sensitivity values and detection ranges between our work and other reported fibre-optic sensing technologies.

strategy for improving the gas-sensing performance of metal oxide/polymer composites [40]. The present study focuses on the intrinsic gas-sensing response mechanism of the heterojunction without additional optical excitation, while the aforementioned photoelectric synergistic mechanism points to a promising direction for the future development of high-performance, room-temperature operated photo-activated gas sensors.

4. Materials and methods

4.1. Materials and reagents

All chemical reagents were of analytical grade and were used without further purification. The SnO_2 dispersion solution was purchased from Aopiweit New Energy Technology Co., Ltd. (Yingkou, China). PANI, NMP and ammonium hydroxide solutions were purchased from Macklin Biochemical Co., Ltd. (Shanghai, China). Ethanol, acetone, toluene, carbinol, isopropanol, and n-hexane solutions were obtained from Sinopharm Chemical Reagent Co., Ltd. (Shanghai, China).

4.2. Morphological characterization

The surface morphologies of microfibre coated with different nano-interfaces were measured by SEM (Regulus 8230, Hitachi, Japan). The analysis of the elemental distribution was performed on an EDX detector (Oxford, Ultim Extreme). XPS measurements were performed using a K-Alpha spectrometer (Thermo Fisher Scientific, USA). FTIR spectra were recorded using an infrared spectrometer (iS10, Thermo Fisher Scientific, USA). Zeta potential measurements were carried out with a Malvern Zetasizer Nano ZS instrument (Malvern Panalytical, UK). The pH values were measured using a pH meter (FE28, Mettler Toledo, Switzerland).

4.3. Experimental setup

Broadband light was launched from a BBS with a power intensity of −25 dBm/nm. An OSA (YOKOGAWA AQ6370D) with a minimum resolution of 0.02 nm was employed to monitor the evolution of the cosine-type transmission spectrum for the optical microfibre device in real time. The optical transmission spectrum signal was recorded by using a data collection card. p-n semiconductor electrical signals were measured via a high-speed multiphysical quantity scanning integrated test system (ScanPro Advance, Nanjing, China).

4.4. Sensing principle of the microfibre

For the optical microfibre, the incident beam can be split into the fundamental mode of HE_{11} and the higher-order mode of HE_{12} in the transition regions for the optical microfibre. Two-mode interference is denoted as follows:

$$I = I_{co} + I_{cl} + 2\sqrt{I_{co} \cdot I_{cl}}\cos(\Delta\phi) \tag{3}$$

where $\Delta\phi = \frac{2\pi L}{\lambda}\left(n_{eff}^{co} - n_{eff}^{cl}\right)$, I_{co} and I_{cl} denote the light intensities of the fundamental mode of HE_{11} and the higher-order mode of HE_{12}, respectively. LMF indicates the interferometric length of the microfibre. The external variation in the refractive index (RI) of the microfibre can induce a wavelength shift, which is determined as follows [41]:

$$\frac{d\lambda}{dn_{ext}} = \lambda \cdot \frac{1}{\gamma} \cdot \left(\frac{1}{\Delta n_{eff}} \cdot \frac{\partial \Delta n_{eff}}{\partial n_{ext}}\right) \tag{4}$$

where $\gamma = 1 - \frac{\lambda}{\Delta n_{eff}} \cdot \frac{d\Delta n_{eff}}{d\lambda}$ indicates the surface RI of the optical microfibre and where Δn_{eff} represents the difference between the effective indices of the fundamental mode of n_{eff}^{co} and n_{eff}^{cl} the higher-order mode for the fibre-optic device.

4.5. Numerical simulations and calculations

The mode distribution of the optical microfibre was simulated by using a commercial COMSOL Multiphysics software via the finite element method (FEM).

5. Conclusions

In conclusion, an optical microfibre coated with an n-type semiconductor of SnO_2 and a p-type semiconductor of PANI was proposed for the detection of ammonia gas at room temperature. On the basis of this novel heterojunction-optical field synergy, the sensor could realize a high sensitivity of 3.98 pm/ppm and an extremely low theoretical LOD of 15.2 ppm. The response/recovery times of the sensor were shortened to 11 s/7 s compared with those of the other methods. Thus, the platform constructed in this work can provide a universal strategy for developing a new generation of high-performance optical-semiconductor hybrid sensing platforms arising, which can be extended to the detection of other gases or biomolecules.

CRediT authorship contribution statement

Hongtao Li: Writing – review & editing, Writing – original draft, Supervision, Resources, Project administration, Investigation, Funding acquisition, Formal analysis, Conceptualization. **Wei Hu:** Writing – original draft, Software, Methodology, Investigation, Formal analysis. **Jiaoyan Dai:** Visualization, Validation, Investigation, Formal analysis. **Shunshuo Cai:** Writing – review & editing, Supervision, Methodology, Investigation. **Lei Huang:** Validation, Investigation, Formal analysis, Data curation. **Liang Lu:** Validation, Investigation, Funding acquisition. **Jialiang Lv:** Visualization, Validation, Formal analysis. **Xue Liu:** Validation, Resources, Formal analysis. **Feng Xu:** Visualization, Validation.

Yujun Li: . **Benli Yu:** Validation, Supervision, Resources. **Christophe Caucheteur:** Visualization, Validation, Project administration, Methodology.

Declaration of competing interest

The authors declare that they have no known competing financial interests or personal relationships that could have appeared to influence the work reported in this paper.

Acknowledgements

This work was supported by the National Natural Science Foundation of China (62105001, 62275001), Natural Science Foundation of Anhui Province (2508085MF162), Natural Science Research Project in Universities of Anhui Province (2024AH050047), Research Funds for Institute of Environmental Hefei Comprehensive National Science Center (HYKYTD2024009).

Data availability

Data will be made available on request.

References

[1] L.L. Du, D.L. Feng, X.X. Xing, C. Wang, Y. Gao, S.H. Sun, G.W. Meng, D.C. Yang, Nanocomposite-decorated filter paper as a twistable and water-tolerant sensor for selective detection of 5 ppb-60 v/v% ammonia, ACS Sens. 7 (3) (2022) 874–883.
[2] X.J. Bai, D. Zhao, H.X. Song, H. He, J.X. Li, L. Hou, Z.T. Li, L.L. Sui, Emerging horizons in gas sensing: exploring the potential of MXenes and MBenes, ACS Appl. Mater. Interfaces 16 (43) (2024) 58060–58071.
[3] V. Chaudhary, N. Ashraf, M. Khalid, R. Walvekar, Y. Yang, A. Kaushik, Y.K. Mishra, Emergence of MXene-polymer hybrid nanocomposites as high-performance next-generation chemiresistors for efficient air quality monitoring, Adv. Funct. Mater. 32 (33) (2022).
[4] S.S. Cai, Y.Y. Ju, Y.M. Wang, X.W. Li, T. Guo, H.Z. Zhong, L.L. Huang, Fast-response oxygen optical fiber sensor based on PEA_2SnI_4 perovskite with extremely low limit of detection, Adv. Sci. 9 (8) (2022).
[5] Z.Y. Yang, X.Y. Yan, B. Peng, Z.C. Li, X.D. Xia, C.H. Lu, D.T. You, K.W. Li, T. Guo, Ultrafast and reproducible fiber-optic hydrogen sensor via a tilted fiber grating with Pd/WO_3 nanocoating, Photon. Sens. 15 (2) (2025).
[6] R. Tabassum, R. Kant, Recent trends in surface plasmon resonance based fiber-optic gas sensors utilizing metal oxides and carbon nanomaterials as functional entities, Sens. Actuat. B-Chem (2020) 310.
[7] T. Wang, L. Zhu, H. Kanda, Ti_3C_2 MXene-TiO_2 hybrid-modified U-bend fiberoptic sensor for improved refractive index sensitivity and ammonia detection, Sens. Actuat. B-Chem. (2023) 393.
[8] Y.N. Wang, Z.Q. Yang, L.Y. Qin, Z.Y. Yuan, J. Li, F.L. Meng, Optical fiber HMS ammonia sensor with cellular-like N-CQDs/$Mg_xZn_{1x}O$ at room temperature, ACS Sens. 9 (11) (2024) 5985–5998.
[9] D.R. Tu, Y.W. Tang, Y.Y. Huang, M.Y. Tang, L.R. Li, Y. Li, M.D. Lu, Z.W. Luo, Y. X. Duan, Next-generation wearable/implanted sensors based on fiber optic and its application: from in vitro to in vivo, ACS Sens. 10 (6) (2025) 3818–3839.
[10] J.D. Lopez-Vargas, A. Dante, R.C. Allil, I. Del Villar, I.R. Matias, M.M. Werneck, Ag@Fe_3O_4-coated U-shaped plastic optical fiber sensor for H_2S detection, Sens. Actuat. B-Chem. 401 (2024).
[11] M.Y. Li, B.B. Lu, K. Xu, C.X. Teng, M.L. He, J.X. Dai, Y.X. Duan, Z.W. Luo, Cascaded Ω-shaped fiber-optic-based LSPR coated with hybridized nanolayers for refractive index and temperature simultaneous measurement, Opt. Lett. 50 (6) (2025) 1803–1806.
[12] K. Swargiary, S. Thaneerat, N. Kongsawang, A.K. Pathak, C. Viphavakit, Highly sensitive and real-time detection of acetone biomarker for diabetes using a ZnO-coated optical fiber sensor, Biosens. Bioelectron. 271 (2025).
[13] I. Del Villar, E. Gonzalez-Valencia, N. Kwietniewski, D. Burnat, D. Armas, E. Pitula, M. Janik, I.R. Matías, A. Giannetti, P. Torres, F. Chiavaioli, M. Smietana, Nano-photonic crystal D-shaped fiber devices for label-free biosensing at the attomolar limit of detection, Adv. Sci. 11 (35) (2024).
[14] P.C. Zhao, K.V. Krishnaiah, L.H. Guo, T.G. Li, H.L. Ho, A.P. Zhang, W. Jin, Ultraminiature optical fiber-tip 3D-microprinted photothermal interferometric gas sensors, Laser Photon. Rev. 18 (9) (2024).
[15] H.T. Li, X. Wang, H. Wu, W.S. Wang, A.Y. Zheng, J. Zhu, L.L. Liang, H.J. Sun, L. Lu, J.L. Lv, Q. Yu, H.Z. Wang, B.L. Yu, Simultaneous noninvasive ultrasensitive detection of prostate specific antigen and lncRNA PCA3 using multiplexed dual optical microfibers with strong plasmonic nanointerfaces, Biosens. Bioelectron. 264 (2024).
[16] H.Y. Liao, Y. Zhao, K.Y. Zheng, H.H. Bao, S.L. Jiang, H.L. Ho, S.F. Gao, Y.Y. Wang, W. Jin, Stimulated Raman photothermal spectroscopy for gas sensing in a hollow-core optical fiber, Optica 11 (12) (2024) 1682–1689.
[17] Q.Q. Wang, H.W. Fu, J.J. Ding, C. Yang, S. Wang, Sensitivity enhanced microfiber interferometer ammonia gas sensor by using WO_3 nanorods coatings, Opt. Laser Technol. 125 (2020).
[18] H.W. Fu, Q.Q. Wang, J.J. Ding, Y. Zhu, M. Zhang, C. Yang, S. Wang, Fe_2O_3 nanotube coating micro-fiber interferometer for ammonia detection, Sens. Actuat. B-Chem. 303 (2020).
[19] D.D. Rong, G. Meng, X.D. Fang, L.B. You, Z.H. Deng, Delafossite $AgAlO_2$ modified long-period grating for highly-sensitive ammonia sensor, Opt. Express 29 (25) (2021) 42005–42019.
[20] H.N. Xu, S.B. Wang, J.H. Jin, Y.F. Duan, S.Q. Yang, Y.N. Tan, Y.H. Feng, Y.T. Du, C. Y. Shen, Y. Zhang, W. Peng, A large-dynamic range conductivity-modulated PANI online analysis and sensing platform for ammonia gas detection using coupled optical probing mode, Sens. Actuat. B-Chem. 418 (2024).
[21] H.Y. Liu, J.T. Cai, L. Zhang, X.W. Shu, Femtosecond laser inscribed small-period long-period fiber grating coated with a nano-assembled polyelectrolyte film for independent sensing of ammonia gas and temperature, Sens. Actuat. B-Chem. 423 (2025).
[22] W.B. Gan, Y.W. Li, T. Liu, Y.T. Yang, B.A. Song, S.X. Dai, T.F. Xu, Y. Wang, T.J. Lin, P.Q. Zhang, Rapid and sensitive detection of ammonia in water by a long period fiber grating sensor coated with sol-gel silica, Opt. Express 30 (19) (2022) 33817–33825.
[23] A.M. Shrivastav, G. Sharma, A.S. Rathore, R. Jha, Hypersensitive and selective interferometric nose for ultratrace ammonia detection with Fast response utilizing PANI@SnO_2 nanocomposite, ACS Photon. 5 (11) (2018) 4402–4412.
[24] D.Z. Zhang, J.F. Wu, P. Li, Y.H. Cao, Room-temperature SO_2 gas-sensing properties based on a metal-doped MoS_2 nanoflower: an experimental and density functional theory investigation, J. Mater. Chem. A 5 (39) (2017) 20666–20677.
[25] D.Y. Wang, D.Z. Zhang, Y. Yang, Q. Mi, J.H. Zhang, L.D. Yu, Multifunctional latex/polytetrafluoroethylene-based triboelectric nanogenerator for self-powered organ-like MXene/metal-organic framework-derived CuO nanohybrid ammonia sensor, ACS Nano 15 (2) (2021) 2911–2919.
[26] D.Z. Zhang, L.N. Zhou, Y. Wu, C.Q. Yang, H. Zhang, Triboelectric nanogenerator for self-powered gas sensing, Small 20 (51) (2024) 21.
[27] D.D. Zhou, Z.J. Kang, X.H. Liu, W.Y. Yan, H.L. Cai, J.Q. Xu, D.Z. Zhang, High sensitivity ammonia QCM sensor based on ZnO nanoflower assisted cellulose acetate-polyaniline composite nanofibers, Sens. Actuat. B-Chem. 392 (2023) 11.
[28] Y. Zhao, Y.X. Liu, Q. Liu, J.C. Zhao, Y.N. Zhang, Room-temperature operated fast reversible ammonia sensor based on hybrid optical fiber structure with temperature compensated function, Sens. Actuat. B-Chem. 408 (2024).
[29] H. Li, K. Yang, H.B. Hu, C.B. Qin, B.L. Yu, S. Zhou, T.T. Jiang, D.R. Ho, MXene supported surface plasmon polaritons for optical microfiber ammonia sensing, Anal. Chem. 96 (29) (2024) 11823–11831.
[30] L.J. Li, M.G. Xue, Q. Ma, X.L. Liu, X.C. Gu, W.Q. Xiu, X. Yang, M.Q. Lv, Graphene/polyaniline film optical fiber ammonia gas sensor with excellent sensing performance, IEEE Sens. J. 23 (14) (2023) 15652–15659.
[31] A. Shokri, N. Salami, Gas sensor based on MoS_2 monolayer, Sens. Actuat. B-Chem. 236 (2016) 378–385.
[32] F. Chiavaioli, C.A.J. Gouveia, P.A.S. Jorge, F. Baldini, Towards a uniform metrological assessment of grating-based optical fiber sensors: from refractometers to biosensors, Biosens.-Basel 7 (2) (2017).
[33] S.S. Cai, Y.G. Nan, Y.H. Li, Y. Hou, Z.C. Zhang, Rapid detection of hydrogen using narrow bandwidth fiber-optic spectral combs with a low limit of detection, Opt. Express 31 (22) (2023) 35616–35623.
[34] Y.H. Dou, C.L. Tang, Y.B. Lu, Self-powered, highly sensitive, and flexible humidity sensor based on carboxymethyl cellulose for multifunctional applications, Langmuir 39 (48) (2023) 17436–17445.
[35] S.A. Sajedi, M.M. Bagheri-Mohagheghi, A. Shirpay, PANI/SnO_2 nanoparticle, FTO/PET and Al/PET as hybrid nanocomposite soft electrodes synthesized by sol-gel, spray pyrolysis and thermal vacuum evaporation methods, Bull. Mater. Sci. 47 (1) (2023).
[36] C. Zhou, H. Yu, M. Yang, X.T. Dong, Y. Yang, CdS/BiOBr photocatalysts modified with monocrystalline Cd quantum dots for sterilization and degradation of organic dyes and antibiotics, ACS Appl. Nano Mater. 8 (25) (2025) 12828–12839.
[37] C.H. Chen, X.W. Zhu, H. Yu, M. Yang, X.T. Dong, Y. Yang, Preparation of dendritic ZnO/Ag-QDs/AgCl photocatalysts and its photodegradation of organic dyes and antibiotics, Solid State Sci. 168 (2025) 12.
[38] W.Y. Li, H. Yu, M. Yang, X.T. Dong, Y. Yang, T.Q. Wang, Natural sunlight excited ZnO/ZIF-8 derivative NOx gas sensor and its application in automobile exhaust gas detection, Sensor. Actuat. B-Chem. 449 (2026) 12.
[39] W.Y. Li, H. Yu, M. Yang, X.T. Dong, Y. Yang, T.Q. Wang, Gas-sensitive performances of Zn/W-PTA derivative composite excited by a single UV-LED, J. Alloys Compd. 1050 (2026) 10.
[40] T. Xue, J.B. Yu, H. Yu, M. Yang, X.T. Dong, Y. Yang, T.Q. Wang, Construction of gas-sensing material with ZnO crystal flower clustered on sea urchin-like CuO structure and its gas-sensing properties to NOx at room temperature, Ceram. Int. 51 (24) (2025) 42806–42814.
[41] Y.Z. Tan, L.P. Sun, L. Jin, J. Li, B.O. Guan, Microfiber Mach-Zehnder interferometer based on long period grating for sensing applications, Opt. Express 21 (1) (2013) 154–164.